$$V = |V_0| \cdot e^{j\,\omega t} \tag{1}$$

which may be rewritten using Euler's formula:

$$V = |V_0| \cdot \{\cos(\omega t) + j \sin(\omega t)\} \tag{1a}$$

For the simple case of a parallel resistor, R, and capacitor, C, the current is

$$I = \frac{V}{R} + C\frac{\partial V}{\partial t} \tag{2}$$

And treating both current and voltage as complex numbers, the admittance, Y, is given by the ratio:

$$Y = \frac{I}{V} = \frac{1}{R} + j\,\omega C \tag{3}$$

Real materials will, in general, display more complicated response than this, with contributions from transport of electrons through the electronic conductors, the polarization of dipoles and multipoles in the sample, and the migration of ions and point defects (interstitials and atomic vacancies) in response to the electric field. The movement of the charge carriers depends on the resistance, and the charge storage on the capacitance of the sample.

It is normally expected that the system under study responds linearly to the applied stimulus, and that all relevant properties of the system are invariant within the timeframe of the experiment. In general, the measured properties will depend on such controllable variables as the temperature, atmosphere (e.g., oxygen or hydrogen partial pressure), and on the applied voltage bias.

Data Analysis, Elements, and Codes

The data resulting from such a measurement (usually a list of f, Z_{re}, Z_{im}) are analyzed using a complex nonlinear least squares (CNLS) fitting code, to determine the parameters of a circuit equivalent. Examples of such codes are *LEVM* written by one of the present authors (Macdonald and Potter, 1987; Macdonald, 2000a) and the first and most comprehensive one (see LEVMW, web information), *EQC* written by B. A. Boukamp, *ZView* from Scribner Associates Inc., *ZSimpWin* from EChem Software, and *MEISP* from Kumho Chemical Laboratories. Each of these codes has its own strengths, and the new user is advised to test the codes, if possible, before committing to one of them. The codes allow a circuit to be built from elements R, C, L, and $\mathcal{Q}$, the constant phase element (see below), as well as several other elements of relevance mainly to electrochemistry. One of the earliest applications of CNLS fitting of dielectric data for liquids appears in Macdonald (1995). The constant phase element (CPE) (Barsoukov and Macdonald, 2005; Macdonald, 1984) deserves special mention. In most software, it is defined by Equation 4

$$Y_{\mathcal{Q}} = Y_0(j\omega)^n \tag{4}$$

where ω is the angular frequency ($\omega \equiv 2\pi f$), and $0 \le n \le 1$. According to this definition, $Y_{\mathcal{Q}}$ has the rather cumbersome units of $S \cdot s^n$.

The element often occurs in parallel combination with a resistor, in which case it can be referred to as a ZARC or ZC element (Macdonald, 2000b). The impedance of this element can be expressed by Equation 5

$$Z = \frac{Z_0}{1 + RY_0(j\omega)^n} \tag{5}$$

Since the ZARC is not equivalent to a parallel (RC) combination (except in the special case of $n = 1$), the parallel capacitance of the ZARC is not constant with frequency. However, a quantity with units of capacitance, C_{qe}, can be derived via Equation 6 (Macdonald, 1984; Hsu and Mansfeld, 2001).

$$C_{qe} = \frac{(RY_0)^{\frac{1}{n}}}{R} \tag{6}$$

In an alternative definition of the CPE,

$$Y_{\mathcal{Q}} = \left(j\,Y_0'\omega\right)^n \tag{7}$$

where Y_0' is an alternative measure of the CPE and Y_0' has units of $S^{1/n} \cdot s$. This definition of the CPE is not available in all impedance analysis codes. The two definitions of the CPE are examined by Jovic (2003) in relation to electrochemical double layer capacitance. The CPE and its relation to other elements involving fractional frequency exponents are discussed by Barsoukov and Macdonald (2012). The usefulness of Equation 6 is that it converts Y_0 to a quasiequivalent capacitance and therefore, has a physical significance. For example, it can be related to the thickness of a polarized layer (bulk, grain boundary, or electrochemical double layer) and is a better alternative than fitting the spectrum to a (RC) circuit.

PRACTICAL ASPECTS OF THE METHOD

Historical Background

Early measurements of impedance were mostly based on the Wheatstone bridge and its several variants, and were made by switching among a set of resistance and capacitance standards until an electrical balance was obtained. The requirement to match the responses of the standards and the sample placed limitations in the range that could be achieved, especially when very large capacitances were concerned. The transformer ratio arm bridge, introduced in the 1940s, eliminated this problem and provided great improvements in measurement stability and precision. As electronics advanced, crystal-controlled synthesizers provided stable measurement frequencies, while phase-sensitive detectors made the task of balancing the bridges much easier. By the 1970s instruments were available that could

measure capacitance and resistance with a resolution of six digits or more. These instruments, however, had a lower limit of a few Hz, due to the difficulty of balancing with such slowly varying signals. By the end of the 1970s, digital gain-phase analyzers had lowered this limit to the mHz range and, by the 1980s, digital impedance analyzers were able to extend this further to a few μHz. As well as wider frequency ranges, these instruments provide increased measurement speed and data acquisition via a computer interface.

When performing measurements on materials, the impedance analyzer is only half of the equipment needed; the other half is the measurement rig, which provides connections to the sample and controls of the temperature and atmosphere. The quality of the measurement will be limited by the part of the system that performs worst. For example, if the conductivity of a sample is highly temperature dependent, inadequate temperature control will invalidate the results, however high the precision of the impedance analyzer. Equally, with a dielectric sample, failure to control the sample environment, for example, humidity, may result in significant errors in the dielectric constant or loss tangent.

Measurement Rigs

In contrast to measurement instruments, which are commercially manufactured, measurement rigs for the determination of conductivity and dielectric constant are usually designed and built in-house; as a result, there are as many designs as there are designers and applications. Two rigs are presented below, which cover different needs depending on the required temperature range: a rig for use near ambient temperature, one for the temperature range −100 to +400°C in vacuum, and one for high temperatures (200–1000°C) in controlled atmospheres.

Figure 1 shows an ambient temperature rig. It is simply constructed, based on an aluminum enclosure. The sample is contacted spring-loaded pins supported on PTFE or nylon insulators and is connected to coaxial connectors on the front. If the measurement instrument allows a two-terminal connection, the rig can be fitted directly, otherwise coaxial cables are used. The rig can be used in the frequency range from dc to several MHz. The lid is sealed by an o-ring, and gas connections can be attached to the two ends if required, to provide a controlled atmosphere, such as dry air. The stray capacitance of this cell is below 0.2 pF.

Figure 2 shows a rig for high temperature and vacuum operation. It is based on a metal block with heating coil. The electrodes contacting the sample are made of steel. The assembly is housed in a vacuum vessel with electrical feedthroughs. A copper rod, brought out via a thin-walled steel tube, dips into a flask with liquid nitrogen to provide cooling. With a controller of suitable range, stable temperatures of −100 to 400°C can be achieved. If measurements below ambient temperature are not required, the liquid nitrogen cooling can be dispensed with. A cell of this design was used to study two different ionic conductors (Lilley and Strutt, 1979; Bonanos and Lilley, 1981) and was found to have a stray capacitance of under 0.5 pF.

When temperatures of 1000°C and above, and controlled chemical environments, are required, rigs must be made of ceramics. Connections to the sample must

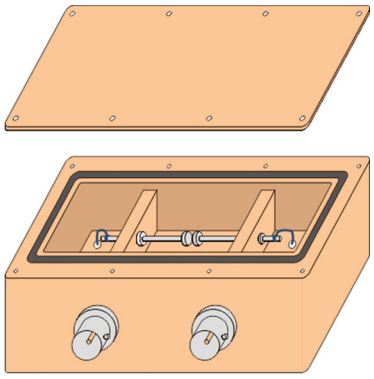

Figure 1. Simple rig designed for measurements at ambient and near-ambient temperature. The sample is contacted by spring-loaded pins. Controlled temperatures of up to ca. 60°C can be achieved using an external resistor heater and thermocouple (not shown). Gas fittings can be added in order to purge the rig with a dry atmosphere.

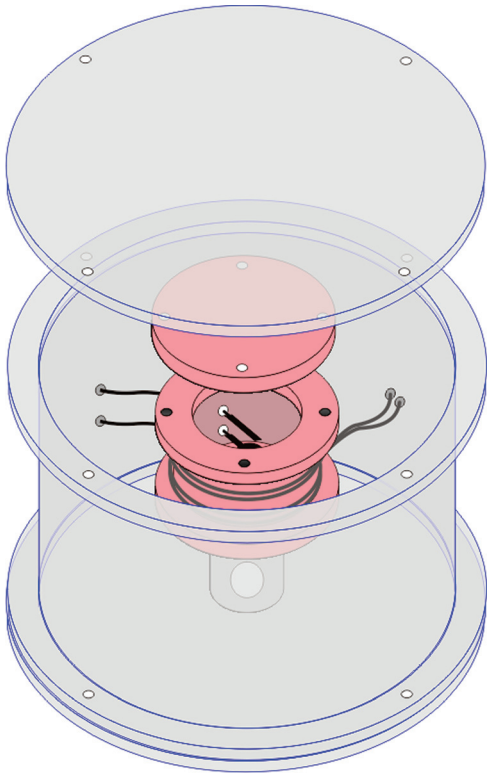

Figure 2. Rig for vacuum operation based on metal block with coaxial heating coil. The electrodes contacting the sample are made of steel spring. With conductive cooling via a copper rod (not shown), stable temperatures of −100 to 400°C can be achieved.

be made via precious metal wires, for example, platinum, as common metals oxidize at such high temperatures. The rig must be enclosed in a tube made of ceramic or silica glass and placed in an electrical tube furnace. A description of such a rig has been given in an earlier publication (Barsoukov and Macdonald, 2005). p. 231.

Considerations of Frequency and Applied Voltage

The bulk response of electroceramics is normally linear and, should be measured using whatever applied voltage is necessary for achieving a good signal-to-noise ratio. On the other hand, the grain boundaries of materials may be nonlinear, as explained in the next section and, when investigating these, the applied voltage is a significant experimental variable. In the authors' experience, the dielectrics literature often passes over the subject of the applied voltage, implicitly assuming that the processes of interest are linear. This is generally correct, but there may be nonlinear processes of a parasitic type. This is illustrated in Figure 3a, which shows the capacitance of a pure Al_2O_3 disc measured at 10 kHz, at ambient temperature, in laboratory air. As can be seen, the capacitance exceeds the geometric capacitance at low applied voltage. This is caused by a layer of adsorbed water providing protonic surface conduction and a double layer capacitance at the rims of the electrodes. The situation can be described by a circuit equivalent ($C_a(R_bC_b)$), shown in the inert. The validity of this circuit is demonstrated in Figure 3b, in which the excess capacitance vanishes at high frequencies. The above measurements were made in the cell shown in Figure 1.

Consequently, when investigating materials of low conductivity, it is advisable to check for possible dependence of the measurements on applied voltage and frequency and to look out for evidence of surface conduction. It is also essential to perform the measurements in/an environment of controlled humidity.

METHOD AUTOMATION

While, in the early days of impedance spectroscopy, component bridges were balanced manually and data were written in notebooks, today any laboratory involved in impedance spectroscopy will have a certain level of automation. In particular, the temperature and atmosphere of the measurement cell would be under computer control and measurements would invariably be stored digitally. Software for controlling impedance analysers is commercially available, but the need for the computer to communicate with different kinds of equipment means that many laboratories still prefer to use in-house written software.

DATA ANALYSIS AND INITIAL INTERPRETATION

Representations in the Complex Plane

Where several relaxation processes are present with different characteristic frequencies, or time constants, they can be resolved in one of various representations in the complex plane. Which one is most suitable depends on whether the processes are envisaged as sequential (e.g., serial connected) or parallel, and also on the relative magnitudes of the components responsible for the conduction and charge storage (normally resistors and capacitors). The impedance spectrum is recommended when processes are sequential and their capacitances differ by orders of magnitude, while the complex capacitance spectrum is recommended when the processes occur in parallel, and the time constants differ due to different resistive components.

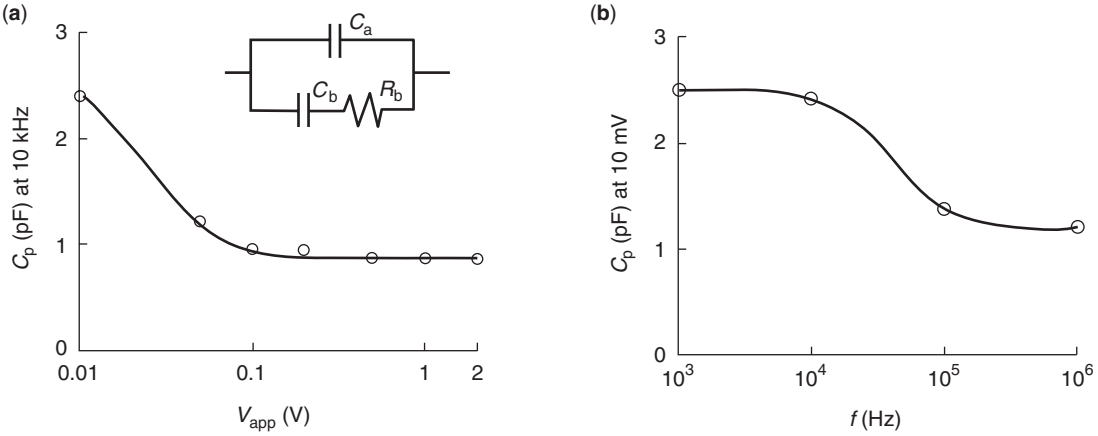

Figure 3. Capacitance of Al_2O_3 disc at room temperature, in laboratory air, measured as a function of (**a**) applied ac voltage at constant frequency and (**b**) measurement frequency at constant voltage. Inset shows the proposed circuit equivalent.

Applications in Electroceramics

In electroceramics, the electrical conductivity of the grain boundary regions, σ_{gb} usually differs from that of grain interiors σ_{gi}, and when this is the case, the polarizations of the two regions appear as distinct features in the impedance spectrum. This can be explained using the so-called *brick layer model* (Beekmans and Heyne, 1976), which is in effect an extension of the Bauerle (1969) model and treats the ceramic as an array of cubic grains, as illustrated in Figure 4a. The model allows two paths available to the current: through grains *and* across grain boundaries or along grain boundaries (Fig. 4b). When $\sigma_{gb} \ll \sigma_{gi}$ the current through the latter path can be ignored and the impedance is the sum of the impedances of the two regions weighted by their relative thickness. In this case, and neglecting possible electrode effects, the material can be treated using a circuit $(R_{gi}C_{gi})(R_{gb}C_{gb})$ (Fig. 4c). In that case, several useful relations hold (Barsoukov and Macdonald, 2005). For the grain interiors, the conductivity, σ_{gi}, and dielectric constant, ε_{gi}, can be obtained directly from the parameters of the circuit equivalent:

$$\sigma_{gi} = \frac{\ell}{A}\frac{1}{R_{gi}} \tag{8}$$

$$\varepsilon'_{gi} = \frac{\ell}{A}\frac{C_{gi}}{\varepsilon_0} \tag{9}$$

where ℓ is the thickness, A the cross-sectional area of the sample, and ε_0 is the permittivity of free space $(8.8542 \times 10^{-16}$ F/m).

If the grain size of the ceramic, and the dielectric constants of both regions, are known, the grain boundary thickness can be obtained from the ratio of the capacitances.

$$d = D\frac{C_{gi}}{C_{gb}}\frac{\varepsilon'_{gb}}{\varepsilon'_{gi}} \tag{10}$$

where D is the grain size, d the grain boundary thickness, and ε'_{gi}, ε'_{gb} are the dielectric constants of the two regions. Further, making the assumptions $\varepsilon'_{gb} = \varepsilon'_{gi}$, the following relation is obtained (Haile et al., 1998). Similar expressions have been derived by others (Vollmann et al., 1997; Waser and Hagenbeck, 2000) in the context of electroceramics.

$$\sigma_{gb} = \frac{\ell}{A}\frac{C_{gi}}{C_{gb}}\frac{1}{R_{gb}} \tag{11}$$

This permits an estimation of the specific conductivity of the grain boundary region, even without knowledge of the grain boundary thickness or grain size. The relation can be very useful as a starting point for an investigation, although it is not a substitute for a microstructural study. Experience has shown that a complete understanding of the properties of electroceramics requires a combination of IS and electron microscopic investigations (Barsoukov and Macdonald, 2005).

In the above, the properties of grain boundaries have been treated phenomenologically, without clearly stating the physical causes of their high impedance. While grain boundary polarization can be caused by second phases, for example, in ionic conductors containing impurities, with electroceramics this seems to be the exception. A large body of work demonstrates that the atomic discontinuities and lower atomic density at the cores of grain boundaries add up to a local electrical charge, which is compensated by an accumulation of charge carriers of the opposite kind around the discontinuity. PTCR electroceramics such as $BaTiO_3$ are normally *n*-type (i.e., oxides doped with an element of valence higher than that of the host). The grain boundary

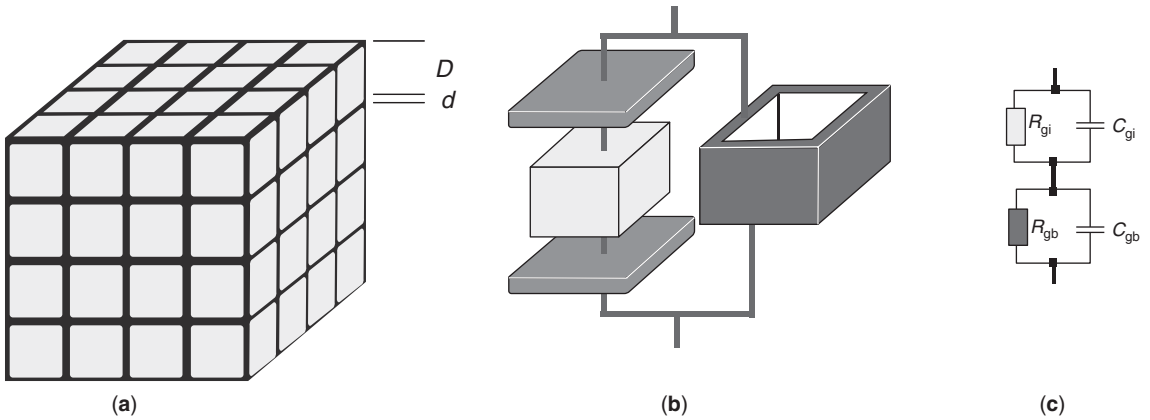

Figure 4. (**a**) Brick layer model treating an electroceramic as an array of cubic grains with planar grain boundaries (Beekmans and Heyne, 1976). (**b**) Available paths for the current through grains, across grain boundaries, and along grain boundaries. (**c**) For $d \gg D$, the model is equivalent to a circuit of type (*RC*)(*RC*).

core acquires a negative charge, which is then compensated by positive carriers in the space near the grain boundary. The result is a local region of diminished conductivity, or depletion layer. With *p*-type electroceramics (doped with a lower valence element) the sign of the layer is reversed, but the conductivity is depleted, as in the case of the *n*-type material.

The total width of the depletion layer on both sides of the grain boundary is given by Waser and Hagenbeck (2000):

$$d_{gb} = \sqrt{\frac{\varepsilon' \Phi_{gb}}{c_\infty}} \qquad (12)$$

where ε' is the dielectric constant of the medium, Φ_{gb} is the height of the potential barrier, and c_∞ is the molar concentration of compensating charges far from the interface.

For a discussion of these concepts, the reader is referred to the comprehensive work of Waser and Hagenbeck (2000) and references therein.

Examples

An example of an impedance spectrum of an electronically conducting ceramic is given in Figure 5. It was obtained on a sample of polycrystalline yttrium iron garnet (YIG), of composition $Y_3Fe_5O_{12}$ measured at 324°C (Vladikova, 2006). The spectrum can be modeled by the circuit (*RQ*)(*RQ*). The resistances for the two elements are shown by the arcs drawn in Figure 5. The capacitances, C_{qe}, when converted to dielectric constants, give values of 38.7 and 909, respectively. The first one is reasonable for an oxide, and allows us to ascribe the relaxation to the grain interior. However, the second one is unrealistically large, indicating that it must be a grain boundary relaxation.

Using Equations 8 and 11, the specific conductivities of the grain interiors and grain boundaries are extracted

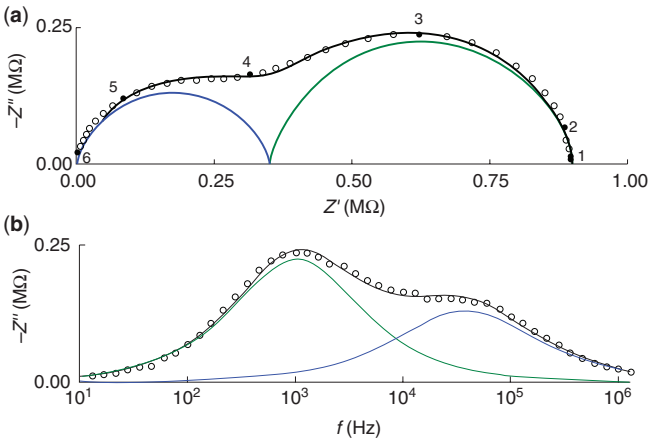

Figure 5. Impedance spectrum of electronically conducting YIG ceramic at 324C. (**a**) Complex plane and (**b**) imaginary part versus frequency. Selected data points in (**a**) are labeled by the logarithm of the frequency. Measurements courtesy

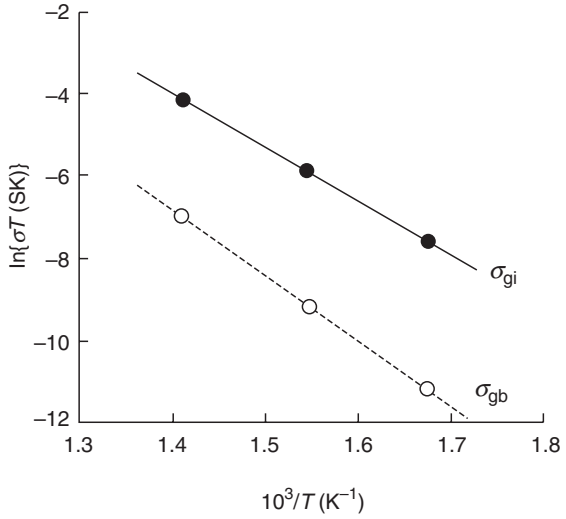

Figure 6. Arrhenius plots for the conductivities for polycrystalline YIG sample whose impedance spectrum is shown in Figure 5.

and plotted in Figure 6, for the temperature range studied. Interpretation of the slopes of the two lines via the Arrhenius Equation 13 indicates a higher activation energy for the grain boundary region, 1.36 eV versus 1.11 eV for the grain interior.

$$\sigma T = A_0 e^{-\frac{\Delta H}{kT}} \qquad (13)$$

A sample of single crystal YIG of similar composition presents a much simpler picture, as shown in Figure 7 for a temperature of 385°C (Vladikova et al., 2004).

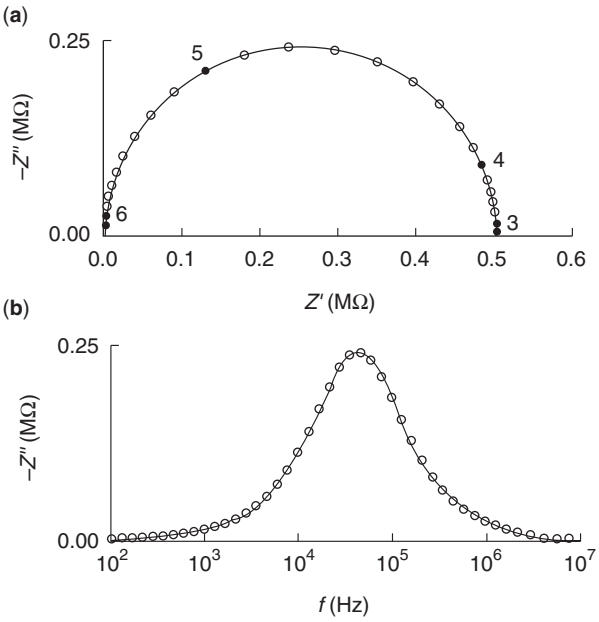

Figure 7. Impedance spectrum of electronically conducting YIG monocrystal at 375C. (**a**) Complex plane and (**b**) imaginary part versus frequency. Selected data points in (**a**) are labeled by the logarithm of the frequency. Courtesy of D. Vladikova and Z. Stoynov, IEES, BAS.

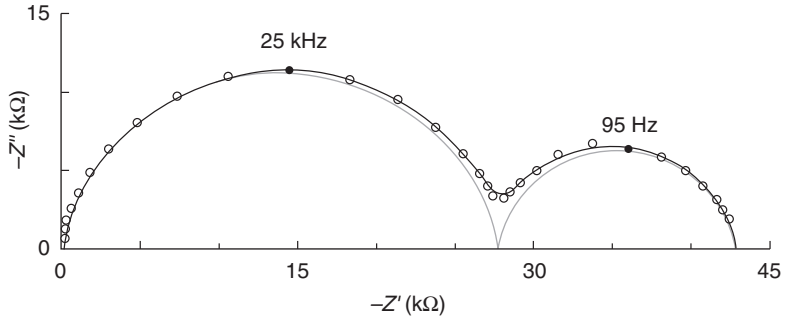

Figure 8. Impedance spectrum for liquid-phase sintered silicon carbide at 250°C, in vacuum, showing resolved grain interior and grain boundary arcs, adapted from McLachlan et al. (2004). The gray lines are the fits to (*RQ*) elements for the grain interior and grain boundary relaxations. (N.B. A frequency-dependent conductivity based on another model was used in the original reference.)

A single arc is observed which can be ascribed to a simple conductivity relaxation of the bulk.

Conductivity relaxations occur also in materials whose use is far removed from ionics or electronics. For example, ceramics of silicon carbide prepared by liquid phase sintering were found to have electrical characteristics resembling those of electroceramics. Figure 8 shows data replotted from the literature (McLachlan et al., 2004), for a fine-grained ceramic ($D < 2\mu$m) at 250°C. The spectrum clearly resolves the grain interior and grain boundary arcs. The grain boundaries consist of several phases, related to the doping of the material (McLachlan et al., 2004).

Experimental studies of seemingly well-understood materials sometimes produce unexpected results. Figure 9 shows an impedance spectrum, at 77.4 K, of $La_{0.58}Sr_{0.4}Co_{0.2}Fe_{0.8}O_3$ (lanthanum strontium cobaltite ferrite, LSCF), an electronically conducting oxide used as a cathode for solid oxide fuel cells. At normal operating temperatures of ca. 600°C, and at ambient temperature, any relaxations that may be present lie outside the frequency range of ordinary impedance analyzers. However, at liquid nitrogen temperature, the sample shows what appears to be a grain boundary relaxation. While this is of no consequence to the operation of a fuel cell, it illustrates the need to explore the widest possible range of experimental conditions in pursuit of a fundamental understanding of materials and systems.

In the remainder of this section, we present examples of application of impedance spectroscopy in the field of dielectrics, also known as Dielectric Spectroscopy.

Polymer Nanocomposites

The first example, to be discussed in some detail, refers to polymer nanocomposites, consisting of a polymeric matrix and inorganic fillers in the nanometer size. These materials have attracted significant interest in recent years, as they exhibit improved properties at much lower filler factors than would be the case with conventional composites (Jancar et al., 2010). For optimizing and controlling that improvement it is essential to understand how polymer dynamics in the nanocomposites is affected by the presence of and interaction with the nanoparticles. The focus in this example is on rubber/silica nanocomposites, with potential applications in the tires industry. Poly(dimethylsiloxane) (PDMS)/silica nanocomposites at various compositions were prepared by sol–gel techniques in the presence of cross-linked PDMS (Fragiadakis et al., 2005). Transmission electron microscopy shows a fine dispersion of spherical silica nanoparticles with a mean diameter of about 10 nm, while infrared spectroscopy reveals hydrogen bonding interactions between the hydroxyls on the silica surface and the oxygens on the backbone of PDMS (Fragiadakis et al., 2005).

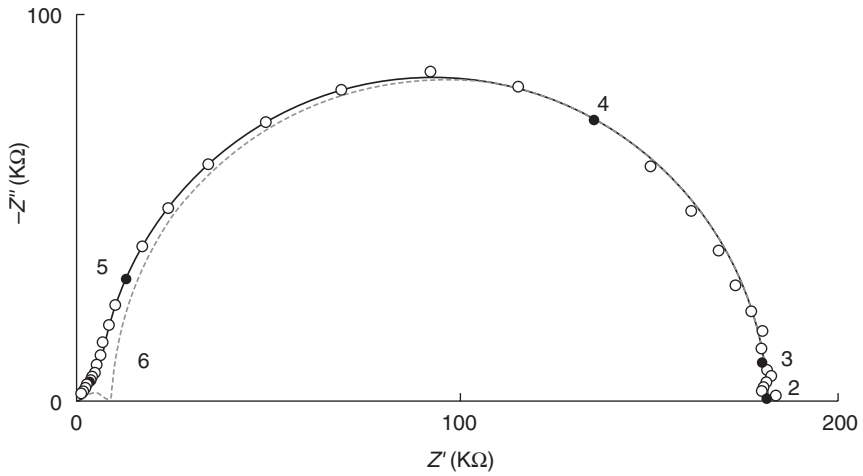

Figure 9. Impedance spectrum of electronically conducting polycrystal of LSCF at 77.4 K (liquid N_2). Selected data points are labeled by the logarithm of the frequency. The gray lines are understood to be grain interior and grain boundary relaxations.

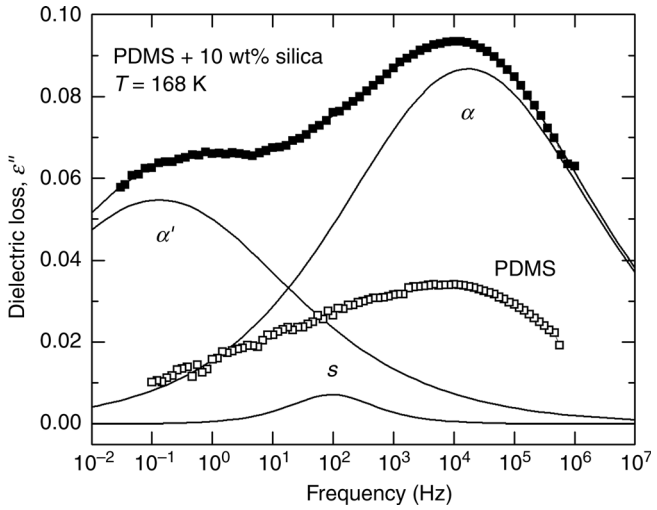

Figure 10. Dielectric loss spectra, $\varepsilon''(f)$, in neat PDMS and a nanocomposite at 168 K (points) and HN analysis of the data in the nanocomposite into a sum of three relaxations (lines).

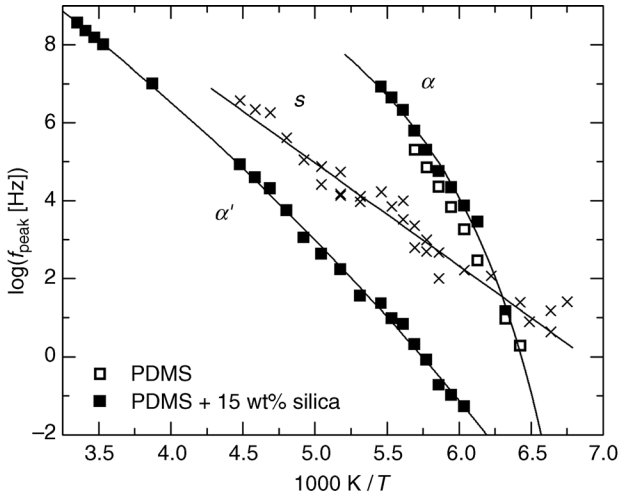

Figure 11. Arrhenius plot for neat PDMS and a nanocomposite. The lines are fits of the Arrhenius Equation 15 and of the VTF Equation 16 to the experimental data for *s*, and for α and α', respectively.

Figure 10 shows dielectric loss spectra in neat PDMS and a nanocomposite at the same temperature, properly selected to follow the segmental α relaxation associated to the glass transition (Fragiadakis et al., 2005), obtained by measuring capacitance and conductance of a plate capacitor filled with the sample (Kremer and Schoenhals, 2002). In neat PDMS, this relaxation gives rise to a single loss peak, shifting to higher frequencies with increasing temperature. The glass transition temperature, T_g, of this material is about 160 K. In the nanocomposite we observe the same loss peak and, in addition, a weaker and slower one, by about five decades in frequency. On the basis of results obtained with several compositions and with other similar systems, we attribute the slower loss peak to the segmental relaxation of polymer chains interacting with the silica nanoparticles, presumably in an interfacial layer around the nanoparticles, and we use the term α' for that. The faster and stronger loss peak, in the same frequency region as in neat PDMS, is, consequently, assigned to the segmental relaxation of PDMS chains sufficiently away from the silica nanoparticles (bulk PDMS) (Fragiadakis et al., 2005).

To quantitatively analyze these and similar experimental results, model functions are fitted to the data, here a sum of Havriliak–Negami (HN) terms, one for each loss peak, of the type (Kremer and Schoenhals, 2002; Barsoukov and Macdonald, 2012).

$$\varepsilon^*(\omega) = \varepsilon_\infty + \frac{\Delta\varepsilon}{[1 + (j\omega\tau)^{1-\alpha}]^\beta} \tag{14}$$

In this expression, $\varepsilon^*(\omega) = \varepsilon'(\omega) - i\varepsilon''(\omega)$ is the complex dielectric function, $\Delta\varepsilon$ is the dielectric strength (dispersion), $\Delta\varepsilon = \varepsilon_s - \varepsilon_\infty$, where ε_s and ε_∞ are respectively the low- and high-frequency limits of ε', τ is the relaxation time, $\tau = 1/2\pi f_{HN}$, where f_{HN} is a characteristic frequency closely related to the loss peak frequency f_{peak}, and α, β are the shape parameters describing the $\varepsilon''(\omega)$ curve. The analysis indicates the existence of a third, weaker relaxation, *s*, as shown in the example of Figure 10, assigned to the rotation of hydroxyl groups attached to the silica surface, confirmed by comparison with literature (Fragiadakis et al., 2005).

Analysis provides information on the time scale, the strength and the shape of each relaxation (Kremer and Schoenhals, 2002; Fragiadakis et al., 2006). Time scale is best discussed in terms of the Arrhenius diagram shown in Figure 11 for neat PDMS and a nanocomposite. The lines are fits of the Arrhenius equation (Fragiadakis et al., 2006):

$$f_{max} = f_o \exp\left(-\frac{\Delta H}{kT}\right) \tag{15}$$

to the data for the local *s* relaxation, and of the Vogel–Tammann–Fulcher (VTF) equation (Fragiadakis et al., 2006)

$$f_{max} = A \exp\left(-\frac{B}{T - T_o}\right) \tag{16}$$

to the data for the cooperative α and α' relaxations. In these equations, ΔH is the activation energy (barrier height), k Boltzmann's constant, f_o and A frequency factors, B a pseudoenergy, and T_o the Vogel temperature (Fragiadakis et al., 2006).

In Figure 12 the temperature dependence of the dielectric strength $\Delta\varepsilon$ of α and α' relaxations is demonstrated for two nanocomposites. These are evaluated as measures of the fractions of bulk and interfacial polymer, respectively (Fragiadakis et al., 2006). The increase of $\Delta\varepsilon$ of α' at the expense of α, with increasing filler content, and the decrease of the former with increasing temperature provide additional support for the assignment of the two relaxations given above.

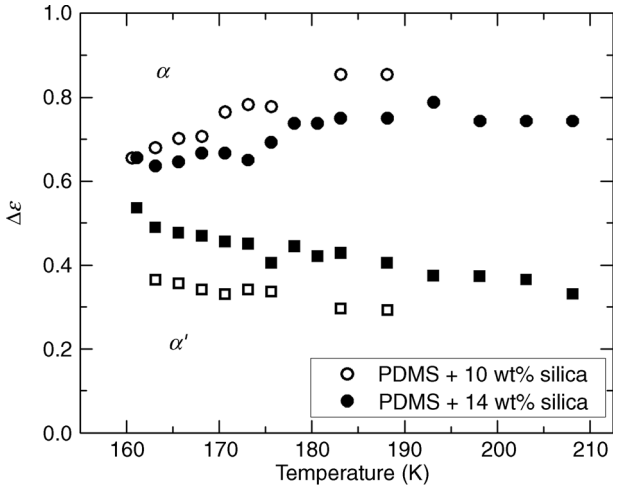

Figure 12. Dielectric strength against temperature for the α and α' relaxations in two PDMS/silica nanocomposites.

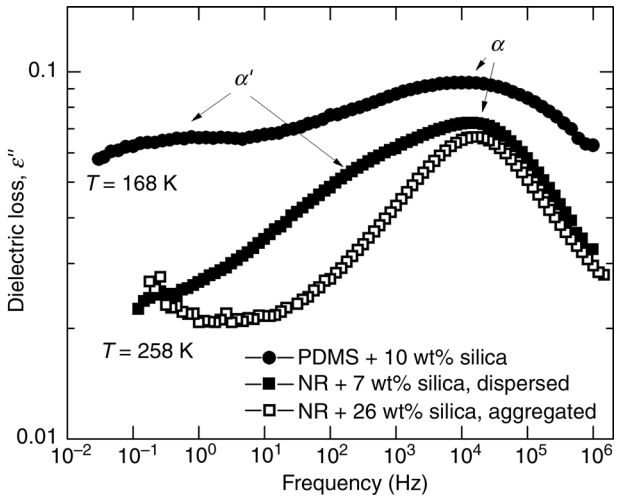

Figure 13. Comparative $\varepsilon''(f)$ spectra in a PDMS and two NR nanocomposites.

In Figure 13 we compare loss spectra in a PDMS and two natural rubber (NR) nanocomposites, one with a fine dispersion of silica nanoparticles, similar to the PDMS nanocomposite, and the second with larger aggregates, in the temperature/frequency regions of the segmental relaxation. Since NR has no oxygens on the backbone, there are no hydrogen bonds in the corresponding silica composites. As a result, the α' relaxation of PDMS/silica becomes a weaker shoulder more close to the α relaxation in the NR nanocomposite with dispersed silica particles, whereas it disappears in the NR nanocomposite with aggregated silica particles, where the surface to volume ratio of the filler decreases significantly.

Application to Block Copolymers

The second example refers to block copolymers. These are polymer chains where two or more types of

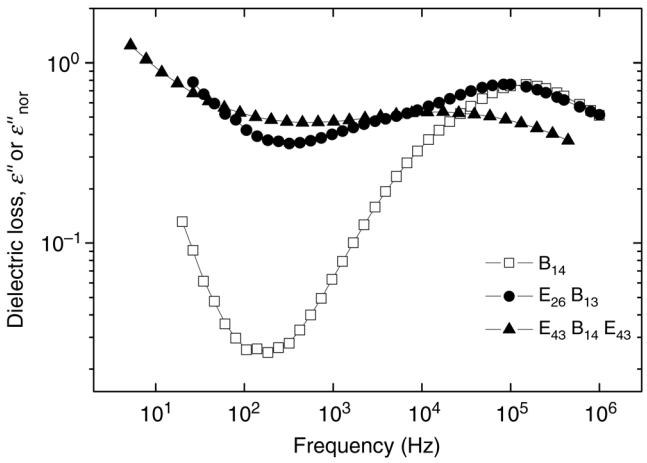

Figure 14. Comparative $\varepsilon''(f)$ spectra recorded with the samples indicated on the plot at 243 K. The ε'' values of the copolymers have been normalized to the volume fraction of B blocks in the sample. The lines are guides to the eye.

monomers are combined in block form, poly(oxybutylene) and poly(oxyethylene) blocks in our example, denoted in the following with B and E, respectively. The useful properties of block copolymers originate largely from the tendency of blocks to segregate, giving rise to microdomain structures (Hamley, 1998). At the low temperatures of measurements employed here, the E blocks crystallize into a lamellar structure (and, thus, do not exhibit long-range molecular mobility), whereas the B blocks are atactic (amorphous). Thus, IS probes select the mobility of the B chains, with constraints imposed by the crystalline E blocks. The B chains possess a dipole moment along the chain axis and exhibit, in addition to the segmental α process, the slower normal mode (NM) process, related to the fluctuation and orientation of the end-to-end polarization vector of the chain (Kyritsis et al., 2000a).

Figure 14 shows comparative dielectric loss spectra in a homopolymer B, a diblock EB, and a triblock EBE, with similar B chain lengths. The indices give the number-average block lengths in chain units. The homopolymer and the triblock are dipole-inverted, growing both ways from the middle of the B chain (Kyritsis et al., 2000a). An example of the analysis by fitting a sum of two HN terms of the type of Equation 14, the faster for the α process and the slower for the NM process, plus a conductivity term, here simultaneously to the ε' and ε'' data, is shown in Figure 15 (Kyritsis et al., 2000a). We already observe in Figure 15 that the α process shows comparable time scale in B and EB, whereas it becomes slower in EBE, reflecting the constraints imposed by tethering both chain ends. Analysis provides quantitative support for that and shows also that the NM process becomes slightly slower in the diblock and significantly slower in the triblock, as compared to the homopolymer, due to effects of fixed chain ends and of dipole inversion (Kyritsis et al., 2000a, 2000b).

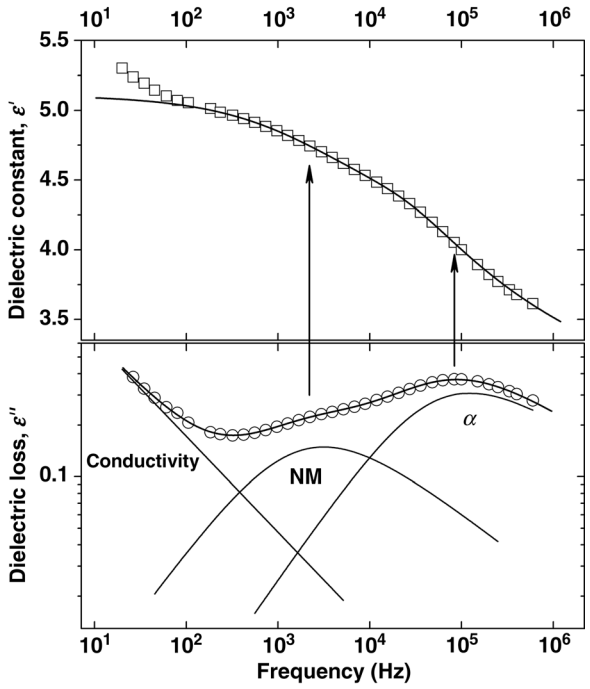

Figure 15. $\varepsilon'(f)$ and $\varepsilon''(f)$ spectra of $E_{26}B_{13}$ at 243 K (points) and analysis into a sum of an α process, a NM process, and a conductivity term (lines).

Dielectric to Conducting Transition

In the third example, we follow the transition from dielectric to conducting behavior with a change in the composition of the sample. Our system is isotactic poly (propylene) (iPP) filled with conducting multiwalled carbon nanotubes (MWCNT). At low filler contents, carbon nanotubes (CNT) are individually dispersed in the polymer matrix and the system shows dielectric behavior (Fig. 16). At higher filler contents, a continuous CNT network is formed and the sample becomes conducting (Fig. 17). The transition can be studied by IS and the percolation threshold p_c, the critical filler content where first macroscopic conductivity appears, can be independently determined by measurements at compositions both lower and higher than p_c. Below p_c, ε' follows the power law (Logakis et al., 2010)

$$\varepsilon' \sim (p_c - p)^{-s} \tag{17}$$

where p is the volume fraction of the filler and s a critical exponent (Fig. 16). The high values of ε', arising from interfacial polarization (Logakis et al., 2010), may be utilized in flexible capacitor and electrostatic dissipation applications. Above p_c, dc conductivity σ_{dc} follows the power law (Logakis et al., 2010).

$$\sigma_{dc} \sim (p - p_c)^t \tag{18}$$

where t is a critical exponent related with the dimensionality of the investigated system (Logakis et al., 2010). σ_{dc} is directly measured or obtained from IS measurements as the plateau (frequency independent) value of ac conductivity σ'_{ac} (actually real part of the complex conductivity) at low frequencies (Fig. 17). In that case, p_c may be determined also from the filler content dependence of the critical frequency of the change from frequency-independent to frequency-dependent conductivity (Logakis et al., 2009). σ'_{ac} is related to ε'' by Logakis et al. (2010).

$$\sigma'_{ac}(\omega) = \varepsilon_o \omega \varepsilon''(\omega) \tag{19}$$

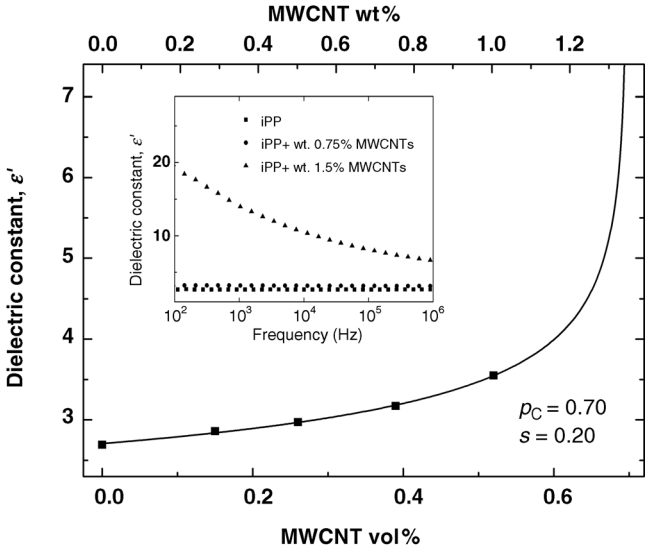

Figure 16. ε' at 1 MHz against vol% (and wt%) filler content in iPP/MWCNT nanocomposites below p_c. The line is a fit of Equation 17 to the data with the fitting parameters given on the plot. The inset shows $\varepsilon'(f)$ for the compositions indicated on the plot.

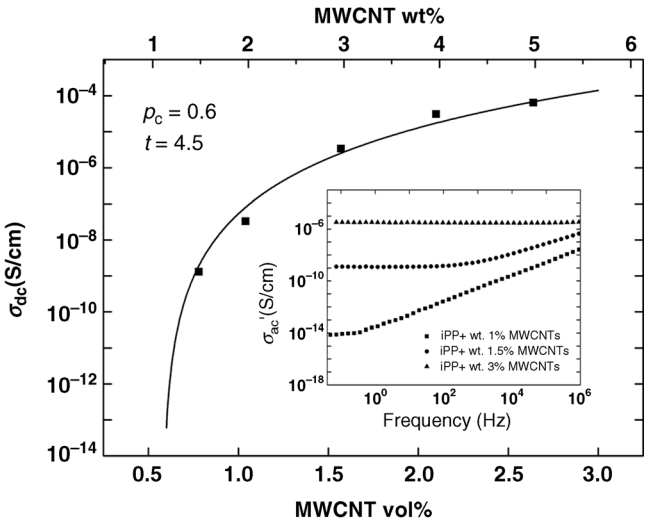

Figure 17. σ_{dc} against vol% (and wt%) filler content in iPP/MWCNT nanocomposites above p_c. The line is a fit of Equation 18 to the data with the fitting parameters given on the plot. The inset shows $\sigma'_{ac}(f)$ for the compositions indicated on the plot.

where ε_o is the permittivity of free space. The high values of conductivity above p_c may be utilized in electrostatic painting, antistatic, and EMI shielding applications.

SAMPLE PREPARATION

Sample Form

The sample, in the form of a flat sheet, is pressed between two capacitor plates. If the sample is not flat enough or is hard (e.g., an electroceramic), metal electrodes are deposited on to the faces, to ensure good electrical contact.

Dimensions

While the dimensions of the sample are not critical, for a given material, the aspect ratio, ℓ/A, affects the magnitude of the sample impedance. Frequently, an ℓ/A of $0.25\,\mathrm{cm}^{-1}$ or less is used, to reduce impedance and, hence, the sensitivity of the measurement to stray capacitance.

Cleaning

If the sample is to be studied at ambient or low temperatures, thorough cleaning and drying is advisable, in order to eliminate the parasitic effects described in Section "Practical Aspects of the Method." For high temperature studies, drying is not essential, as contamination by moisture gases is normally removed during the initial heating.

Electrodes

In contrast to the case of electrochemical impedance spectroscopy, where the electrodes take part in the electrochemical processes, for impedance spectroscopy of dielectrics and electronic conductors, the electrodes serve mainly as current collectors. Electrodes of silver, gold, platinum, palladium, nickel, or carbon are chosen, depending on their chemical compatibility with the sample and the preferred method of deposition: evaporation, sputtering, screen printing, or hand painting.

PROBLEMS

Stray Quantities and Correction for their Effects

The measurements obtained are the combined response of the sample and of the rig. To obtain the response of the sample alone, stray (parasitic) quantities must be estimated and their effect subtracted out of the measured impedance. In practice, the most important stray quantities are the series inductance and the parallel capacitance and these can be reduced by attention to rig design, but cannot be entirely eliminated. The stray inductance can be reduced by making lead lengths as short as possible, while the stray capacitance can be minimized by using screened conductors wherever possible and by grounding any metal parts of the rig.

The stray series inductance, L_{ss}, is evaluated by short circuiting the rig at the position of the sample and performing a measurement in the highest accessible frequency range. If the instrument can display the series inductance, this can be read directly; otherwise it must be obtained by fitting the impedance spectrum to a circuit *RL*, in which the component *R* accounts for the contact resistance. Data obtained with the sample in place are corrected for L_{ss} by subtracting $2\pi f L_{ss}$ from the imaginary part of the impedance, Z_{im}. The stray parallel capacitance, C_{sp}, is evaluated by measurement of the empty rig with the contacts set to their maximum distance, so as to minimize the air gap capacitance, as distinct from stray capacitance. As before, C_{sp} may be read directly from the instrument, or evaluated by fitting to a parallel circuit (*RC*). To correct for C_{sp}, the quantity $2\pi f C_{sp}$ is subtracted from the imaginary part of the admittance. In the above corrections, the real part of the impedance/admittance is not corrected.

As illustrated in the "Data Analysis and Initial Interpretation" section, experimental studies of seemingly well-understood materials sometimes produce unexpected results. The range of experimental conditions explores should always be wider than that of the application, in order to reveal effects that are insignificant at operating conditions. This also leads to a better understanding of materials processes and systems.

CLOSING REMARKS

In the previous sections, we have discussed impedance spectroscopy and its application to selected electronic conducting and dielectric materials. With a few exceptions, the examples have concerned samples and data, about which we have had some background knowledge. While this may have somewhat restricted the range of materials we could cover, we hope that it has illustrated the insight that impedance spectroscopy can bring into solid-state research. We also hope that the examples have emphasized the importance of the control of the experimental conditions, especially of temperature, pressure, humidity, and amplitude of the applied signal.

The examples given reveal two dichotomies regarding the use of IS. The first one concerns the type of circuit (series or parallel) used to model the impedance response:

i. For electroceramics, which according to the brick layer model, for $d << D$ and $\sigma_{gb} << \sigma_{gi}$, are approximated by grain and grain boundary regions connected in series, the preferred representation is the impedance spectrum.
ii. For dielectrics, where relaxation processes occur in parallel (e.g., different dipolar species reorient in response to an applied voltage) the preferred representation is the complex dielectric constant.

The above differences are a reflection of the physical processes and are, therefore, intuitive.

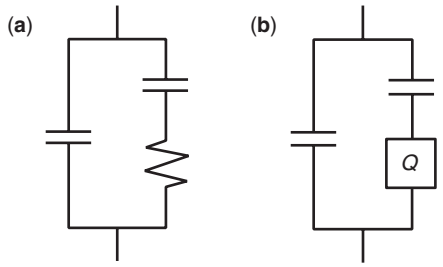

Figure 18. Circuit equivalents for (**a**) the Debye and (**b**) Cole–Cole model of dielectric relaxation.

The second dichotomy concerns the manner in which nonideality is accommodated. In the case of electroceramics and ceramic ionic conductors, this is done by assigning a fractional frequency dependence to the storage element, typically a CPE with $0.5 < n < 1$. Although, as stated by Barsoukov and Macdonald (2012), the CPE has no physical basis, it is rather successful in covering the phenomenology of conductivity relaxation. We also saw that a quasiequivalent capacitance could be derived using Equation 6 and that this quantity has a practical use in determining the length scale of the feature giving rise to the capacitance.

While the literature on dielectrics is not as preoccupied with circuit equivalents as that on ceramics, when nonideality is introduced, it is done via the loss element rather than the storage element (i.e., the resistor rather than the capacitor). The "ideal" Debye model is equivalent to the circuit in Figure 18a, while the Cole–Cole model corresponds to Figure 18b. In other words, the fractional frequency dependence is assigned to the component that replaces the resistor.

The two interpretations function well in isolation from each other. It is, however, not clear how they should be combined when systems exhibit behavior intermediate between conductive and dielectric. Can one, for example, fully account for electroceramics at low temperatures, where the conductivity becomes very low but dielectric properties remain? The next few years will show whether practitioners in dielectrics, electroceramics, and ionics are able to develop unified models for the response of this group of materials.

ACKNOWLEDGMENTS

Coworkers past and present are thanked for many valuable discussions on the theory and practice of impedance spectroscopy. D. Vladikova and Z. Stoynov of the Institute of Electrochemistry and Energy Systems, Bulgarian Academy of Sciences, are specially thanked for providing the original data on YIG. P. Plonczak of Risø DTU collaborated on the study of LCSF.

ABBREVIATIONS

CNLS	complex nonlinear least squares
CNT	carbon nanotubes
CPE	constant phase element
EIS	electrochemical impedance spectroscopy
HN	Havriliak–Negami
iPP	isotactic poly(propylene)
IS	impedance spectroscopy
LSCF	lanthanum strontium cobaltite ferrite
MWCNT	multiwalled carbon nanotubes
NR	natural rubber
PDMS	poly(dimethylsiloxane)
PTCR	positive temperature coefficient of resistance
TSDC	thermally stimulated depolarization currents
VTF	Vogel–Tammann–Fulcher
YIG	yttrium iron garnet
ZARC	impedance element consisting of a resistor and CPE in parallel

SYMBOLS

V	voltage
R	electrical resistance
I	electrical current
C	capacitance
C_{qe}	quasiequivalent capacitance (or pseudocapacitance) for a ZARC
Y	admittance
Z	impedance
Y_0, Y_0'	prefactors in the admittance of the constant phase angle element
n	exponent in the admittance of the constant phase angle element
σ	electrical conductivity
σ_{gi}	grain interior conductivity
σ_{gb}	grain boundary conductivity
R_{gi}	grain interior resistance
R_{gb}	grain boundary resistance
C_{gi}	grain interior capacitance
C_{gb}	grain boundary capacitance
ε_{gi}	grain interior dielectric constant
ε_{gb}	grain boundary dielectric constant
D	grain size
d_{gb}	grain boundary thickness
Φ_{gb}	grain boundary potential barrier
c_∞	defect concentration far from grain boundary core
ΔH	activation energy
A_0	pre-exponential of the electrical conductivity
T_g	glass transition temperature
ε^*	complex dielectric function
ε'	real part of the dielectric function
ε''	imaginary part of the dielectric function (dielectric loss)
ω	angular frequency
$\Delta\varepsilon$	dielectric strength
ε_s	low-frequency limit of the real part of the dielectric function
ε_∞	high-frequency limit of the real part of the dielectric function
τ	relaxation time
f_{HN}	characteristic frequency in the HN Equation 14
f_{peak}	loss peak frequency

α, β	shape parameters
T	absolute temperature
k	Boltzmann's constant
f_o, A	frequency factors
B	pseudoenergy
T_o	Vogel temperature
p_c	percolation threshold
p	filler volume fraction
s	critical exponents
σ_{dc}	dc conductivity
σ'_{ac}	ac conductivity (real part)
ε_0	permittivity of free space

LITERATURE CITED

Barsoukov, E. and Macdonald, J. R. 2005. Impedance Spectroscopy. 2nd ed. Wiley, Hoboken, NJ.

Barsoukov, E. and Macdonald, J. R. 2012. Electrochemical Impedance Spectroscopy This volume.

Bauerle, J. E. 1969. Study of solid electrolyte polarization by a complex admittance method. *J. Phys. Chem. Solids* 30:2657–2670.

Beekmans, N. M. and Heyne, L. 1976. Correlation between impedance, microstructure and composition of calcia-stabilized zirconia. *Electrochim. Acta* 21 303–310.

Bonanos, N. and Lilley, E. 1981. Conductivity relaxations in single crystals of sodium chloride containing suzuki phase precipitates. *J. Phys. Chem. Solids* 42:943–952.

Bucci, C., Fieschi, R., and Guidi, G. 1966. Ionic thermocurrents in dielectrics. *Phys. Rev.* 148:816–823.

Debye, P. J. W. 1929. Polar Molecules. Dover Publications, (original publication 1929).

Fabregat-Santiago, F., Garcia-Belmonte, G., Mora-Seró, I., and Bisquert, J. 2011. Characterization of nanostructured hybrid and organic solar cells by impedance spectroscopy. *Phys. Chem. Chem. Phys.* 13:9083–9118.

Fragiadakis, D., Pissis, P., and Bokobza, L. 2005. Glass transition and molecular dynamics in poly (dimethylsiloxane)/silica nanocomposites. *Polymer* 46:6001–6008.

Fragiadakis, D., Pissis, P., and Bokobza, L. 2006. Modified chain dynamics in poly(dimethylsiloxane)/silica nanocomposites. *J. Non-Cryst. Solids* 352:4969–4972.

Haile, S. M., West, D. L., and Campbell, J. 1998. The role of microstructure and processing on the proton conducting properties of gadolinium-doped barium cerate. *J. Mater. Res.* 13:1576–1595.

Hamley, I. W. 1998. The Physics of Block Copolymers. Oxford University Press, Oxford.

Hodge, I. M., Ingram, M. D., and West, A. R. 1975. New method for analyzing ac behavior of polycrystalline solid electrolytes. *J. Electroanal. Chem.* 58:429–432.

Hong, C-M. and Day, D. E. 1979. Thermally stimulated polarization and depolarization current (TSPC–TSDC) techniques for studying ion motion in glass. *J. Mater. Sci.* 14:2493–2499.

Hsu, C. H. and Mansfeld, F. 2001. Concerning the conversion of the constant phase element parameter Y0 into a capacitance. *Corrosion* 57:747–748.

Irvine, J. T. S., Sinclair, D. C., and West, A. R. 1990. Electroceramics: characterization by impedance spectroscopy. *Adv. Mater.* 2:132–138.

Jancar, J., Douglas, J. F., Starr, F. W., Kumar, S. K., Cassagnau, P., Lesser, A. J., Sternstein, S. S., and Buehler, M. J. 2010. Current issues in research on structure–property relationships in polymer nanocomposites. *Polymer* 51:3321–3343.

Jovic, V. D. 2003. *Research Solutions and Resources*. Available at http://www.consultrsr.com/files/jovic.pdf. Accessed November 29, 2011.

Kremer, F. and Schoenhals, A. 2002. Broadband Dielectric Spectroscopy. Springer, Berlin.

Krohns, S., Lunkenheimer, P., Ebbinghaus, S. G., and Loidl, A. 2007. Broadband dielectric spectroscopy on single-crystalline and ceramic $CaCu_3Ti_4O_{12}$. *Appl. Phys. Lett.* 91:022910.

Kyritsis, A., Pissis, P., Konsta, A., Mai, S.-M., and Booth, C. 2000a. Molecular dynamics in homo, diblock and triblock polymers studied by dielectric relaxation spectroscopy. *IEEE Trans. Diel. El. Insul.* 7:509–516.

Kyritsis, A., Pissis, P., Mai, S.-M., and Booth, C. 2000b. Comparative dielectric studies of segmental and normal mode dynamics of poly(oxybutylene) and poly(oxyethylene)–-poly(oxybutylene) diblock copolymers. *Macromolecules* 33:4581–4595.

LEVMW, web information. The newest WINDOWS version, LEVMW, of the comprehensive LEVM fitting and inversion program may be downloaded at no cost by accessing http://jrossmacdonald.com. Accessed November 29, 2011.

Lilley, E. and Strutt, J. E. 1979. Bulk and grain-boundary ionic-conductivity in polycrystalline beta"-alumina. *Phys. Stat. Sol. A* 54:639–650.

Logakis, E., Pandis, Ch., Peoglos, V., Pissis, P., Piontek, J., Poetschke, P., Micusik, M., and Omastova, M. 2009. Electrical/dielectric properties and conduction mechanism in melt processed polyamide/multi-walled carbon nanotubes composites. *Polymer* 50:5103–5111.

Logakis, E., Pollatos, E., Pandis, Ch., Peoglos, V., Zuburtikudis, I., Delides, C. G., Vatalis, A., Gjoka, M., Syskakis, E., Viras, K., and Pissis, P. 2010. Structure–property relationships in isotactic polypropylene/multi-walled carbon nanotubes nanocomposites. *Compos. Sci. Technol.* 70:328–335.

Macdonald, J. R. 1984. Note on the parameterization of the constant-phase admittance element. *Solid State Ionics* 13:147–149.

Macdonald, J. R. 1995. Exact and approximate nonlinear least-squares inversion of dielectric-relaxation spectra. *J. Chem. Phys.* 102:6241–6250.

Macdonald, J. R. 2000a. Comparison of parametric and nonparametric methods for the analysis and inversion of immittance data: critique of earlier work. *J. Comput. Phys.* 157:280–301.

Macdonald, J. R. 2000b. Comparison of the universal dynamic response power–law fitting model for conducting systems with superior alternative models. *Solid State Ionics* 133:79–97.

Macdonald, J. R. 2011. Effects of various boundary conditions on the response of Poisson–Nernst–Planck impedance spectroscopy analysis models and comparison with a continuous-time random-walk model. *J. Phys. Chem. A* 115:13370–13380.

Macdonald, J. R., Evangelista, L. R., Lenzi, E. K., and Barbero, G. 2011. Comparison of impedance spectroscopy expressions and responses of alternate anomalous Poisson–Nernst–Planck diffusion equations for finite-length situations. *J. Phys. Chem. C* 115:7648–7655.

Macdonald, J. R. and Potter, L. D. Jr. 1987. A flexible procedure for analyzing impedance spectroscopy results: description and illustrations. *Solid State Ionics* 24:61–79.

McLachlan, D. S., Sauti, G., Vorster, A., and Hermann, M. 2004. Impedance spectroscopy of liquid-phase sintered silicon carbide. AIP Conference Proceedings. 700, pp. 1122–1128.

Orazem, M. E. and Tribollet, B. 2008. Electrochemical Impedance Spectroscopy. Wiley, Hoboken, NJ.

Vladikova, D. 2006. Development of differential impedance analysis for investigation of electroceramic systems. D. Sc. Thesis, Institute of Electrochemistry and Energy Systems. Bulgarian Academy of Sciences, Sofia.

Vladikova, D., Stoynov, Z., and Viviani, M. 2004. Application of the differential impedance analysis for investigation of electroceramics. *J. Eur. Ceram. Soc.* 24:1121–1127.

Vollmann, M., Hagenbeck, R., and Waser, R. 1997. Grain-boundary defect chemistry of acceptor-doped titanates: inversion layer and low-field conduction. *J. Am. Ceram. Soc.* 80:2301–2314.

Von Hippel, A. R. 1954. Dielectrics and Waves. Wiley.

Waser, R. and Hagenbeck, R. 2000. Grain boundaries in dielectric and mixed conducting ceramics. *Acta Mater.* 48:797–825.

KEY REFERENCES

Barsoukov, E. and Macdonald, J. R. 2012. ELECTROCHEMICAL IMPEDANCE SPECTROSCOPY in this volume.

Appearing in the same series as the present one, this article rigorously treats electrochemical impedance, including measurements, analysis of data, and electrochemical models. The article contains an up-to date overview of measurement systems.

Barsoukov, E. and Macdonald, J. R. 2005. Impedance Spectroscopy. 2nd ed. Wiley, Hoboken, NJ.

The first monograph dedicated to impedance spectroscopy and a valuable reference work for the middle to advanced user. The subjects covered are theory, measuring techniques, data analysis, for a wide range of electrochemical cells, dielectrics, and solid-state devices, including electrochemical sensors, fuel cells, and batteries.

Orazem, M. E. and Tribollet, B. 2008. Electrochemical Impedance Spectroscopy. Wiley, Hoboken, NJ.

Written for those intending to use impedance spectroscopy in an electrochemical context, the book covers aqueous electrochemistry and corrosion, while also dealing extensively with semiconductors, sensors, electrochromics, batteries, fuel cells, electrochemical capacitors, and dielectrics. The emphasis is on generally applicable fundamentals and is suited for use as a textbook for a university level course or for independent self-study.

Von Hippel, A. R. 1954. Dielectrics and Waves. Wiley.

Published half a century ago and still in print, the book discusses the role played by electromagnetic and elastic waves in solid and liquid dielectrics, piezoelectrics and ferroelectrics, and in magnetic materials. The work is presented both at the macroscopic and the microscopic levels. Considered a classic in its field.